Measurement of thermally ablated lesions in sonoelastographic images using level set methods

Benjamin Castaneda*[a], Jose Gerardo Tamez-Pena[b], Man Zhang[a], Kenneth Hoyt[a], Kevin Bylund[c], Jared Christensen[c], Wael Saad[c], John Strang[c], Deborah J. Rubens[c], Kevin J. Parker[a]
[a]Department of Electrical & Computer Eng., University of Rochester, Rochester, NY, USA 14627; [b]20 Devonwood Ln, Pittsford, Rochester, NY, USA 14534; [c]Department of Imaging Sciences, University of Rochester Medical Center, Rochester, NY, USA 14642

ABSTRACT

The capability of sonoelastography to detect lesions based on elasticity contrast can be applied to monitor the creation of thermally ablated lesion. Currently, segmentation of lesions depicted in sonoelastographic images is performed manually which can be a time consuming process and prone to significant intra- and inter-observer variability. This work presents a semi-automated segmentation algorithm for sonoelastographic data. The user starts by planting a seed in the perceived center of the lesion. Fast marching methods use this information to create an initial estimate of the lesion. Subsequently, level set methods refine its final shape by attaching the segmented contour to edges in the image while maintaining smoothness. The algorithm is applied to *in vivo* sonoelastographic images from twenty five thermal ablated lesions created in porcine livers. The estimated area is compared to results from manual segmentation and gross pathology images. Results show that the algorithm outperforms manual segmentation in accuracy, inter- and intra-observer variability. The processing time per image is significantly reduced.

Keywords: Elasticity, sonoelastography, image processing, segmentation, region growing, fast marching methods, level set methods, Mumford-Shah functional

1. INTRODUCTION

Thermal ablation techniques such as radiofrequency ablation (RFA) and high intensity focused ultrasound (HIFU) have attracted the interest of the research community for their capabilities to treat tumors as minimally invasive techniques [1,2]. In particular, promising results have been reported in early clinical trials for the treatment of hepatic tumors [3,4]. Imaging modalities that dynamically and precisely monitor the lesion during and after the treatment are crucial for the success of thermal ablation therapies.

Ultrasound (US) is generally used for imaging guidance during the ablation procedures. It offers convenient real-time guidance of RFA needle placement, and it has the advantage of being cost-effective and readily available in most clinical sites. However, as an imaging modality to monitor the creation of the lesions, US did not exhibit good results [3]. Besides the low intrinsic contrast between treated and untreated tissues, artifacts due to the gas bubbles created during the treatment appear as hyper-echoic formations [5]. These formations do not represent accurately the extent of ablation. Gas bubbles resolve gradually, resulting in underestimation of the lesion size. On the other hand, MRI capabilities on resolving soft tissues can be used to discriminate thermally ablated from healthy tissue [6], but the procedure becomes expensive and time consuming. Contrast enhanced CT imaging has also been proposed [7]. In this modality, thermally ablated lesions are depicted as hypo-attenuating regions. However, it also presents disadvantages such as ionizing radiation exposure, CT contrast agents' side effects, and extended time of the procedure.

Thermally ablated lesions present an elevated elasticity modulus when compared to the surrounding tissue. Consequently, elasticity imaging modalities have been proposed as an alternative to monitor lesion creation and follow-up [8,9]. In particular, sonoelastography [10] is an imaging technique that estimates the peak displacement of the tissue under an externally induced mechanical harmonic excitation [11]. In a previous study, sonoelastography was used to detect and measure thermal lesions *in vivo* in exposed-liver experiments [5]. Manual measurement of these lesions in the sonoelastographic images is challenging due to diffuse boundary definition and artifacts formed by respiratory motion and perfusion. As a result, outlining and measuring the lesions becomes a time-consuming process with high variability.

*castaned@ece.rochester.edu; phone 1 585 748-3744; fax 1 585 273-4919

Medical Imaging 2008: Ultrasonic Imaging and Signal Processing, edited by Stephen A. McAleavey, Jan D'hooge, Proc. of SPIE Vol. 6920, 692018, (2008) · 1605-7422/08/$18 · doi: 10.1117/12.770811

Although several methods have been proposed to segment US images, only a few techniques have focused on elasticity images. Fahey et al. proposed the application of a simple threshold to acoustic radiation force impulse elastograms [12] with good result in phantom materials due to the high contrast between the inclusion and the background. Techavipoo et al. [13] proposed a semi-automated segmentation algorithm of thermal lesions for compression elastography images. The algorithm was based on thresholding and morphological operations and was applied to *in vitro* RFA lesions. Later, an automated algorithm was reported by the same group [14]. The approach consisted of a coarse-to-fine method which was initialized by template matching and then refined by an active contour model. This technique was evaluated in 2D and 3D *in vitro* elastograms and a proof of concept was shown for 2D *in vivo* images.

The purpose of this paper is to describe a semi-automated algorithm for segmentation of thermal ablated lesions from 2D *in vivo* sonoelastographic images. The proposed algorithm is based on level set techniques which are initialized using fast marching methods. The parameters for the algorithm are selected using the Mumford Shah functional [15]. The performance of the algorithm is compared against manual segmentation and data from gross pathology.

2. ALGORITHM DESCRIPTION

The overall diagram of the proposed algorithm is presented in Fig. 1a. The input image is first pre-processed in order to enhanced its contrast and reduce the effect of uneven illumination. Subsequently, the user initializes the algorithm by selecting the center of the lesion. This input is used as the seed for a fast-marching method that will output an initial guess of the segmentation of the lesion. A level set technique is then applied to refine the initial guess. This step is repeated several times varying the parameters of the level set. Each result is evaluated using the Mumford-Shah functional which finally decides the output of the algorithm.

2.1 Pre-processing

The pre-processing stage consists of several steps shown in Fig. 1b. First, the size of the image is reduced to match the resolution of sonoelastographic images. For the purposes of our experiments, the resolution of the images is approximately 1mm in the axial and lateral directions. Histogram stretching is then applied. Normalization of the histogram of the image reduces the range of parameters to search in following stages. To reduce the effect of noise and uneven illumination in the images, anisotropic diffusion [16] and homomorphic [17] filters are used.

2.2 Fast marching method

The Fast marching method [18] is a numerical form to solve the boundary value problem defined by:

$$F(x)\left|\nabla T(x)\right| = 1 \tag{1}$$

where *F(x)* is the speed function and *T(x)* is the time of arrival function. Given an interface which is always evolving in one direction (outwards or inwards), *T(x)* describes the time in which the front of the interface will arrive to location *x* given the speed function *F(x)*. The latter function describes the speed of the front at a given location and (1) establishes the relationship between them. For the proposed algorithm, *F(x)* is built from the image *I(x)* to be segmented as:

$$F(x) = \frac{1}{1 + e^{-\left|\nabla I(x)\right|}} \tag{2}$$

The user inputs the position of the seed for which *T(x)=0*.

2.3 Threshold Level Set segmentation

Level set methods [18,19] are numerical techniques for tracking the evolution of interfaces (contours or surfaces). The interface is embedded as the zero level set of a higher dimensional function called the level set function $\Psi(x,t)$. This function is then evolved and its behavior is defined by the following differential equation in a general case:

$$\frac{d}{dt}\Psi = -\alpha A(x).\nabla\Psi - \beta P(x)\left|\nabla\Psi\right| + \gamma C(x)\kappa\left|\nabla\Psi\right| = 0 \tag{3}$$

Where A is an advection term, P is a propagation term, and C is a spatial modifier term for the mean curvature κ. The scalar constants α, β, and γ are weights that determine the relative influence of each of the terms on the evolution of the

interface. The evolving interface is obtained at any given time iteration by extracting the zero level set from the higher dimensional function. The main advantages of these techniques are that arbitrarily complex shapes can be modeled and topological changes are handled implicitly.

In the case of threshold level set methods, the propagation term is calculated as:

$$P(x) = \begin{cases} I(x), \ if \ I(x) < U/2 \\ U - I(x), \quad otherwise \end{cases} \tag{4}$$

where U is the threshold which controls whether the interface grows or contracts. The final segmentation of the image is influenced by the intensity value of the sonoelastographic image and the smoothness of the contour. For our experiments γ was set to 50, β was set to 1 and α was set to 0 since the advection term is not required. The high weight for the curvature term is required to avoid leakage in the contour at places where the lesion edge is not well defined.

2.4 Mumford Shah functional

For an image $I(x)$ and a contour $\Gamma(x)$, a simplified version of the Mumford Shah functional [15] for the segmentation of an image in two regions is expressed as:

$$M(I(x),\Gamma(x)) = \upsilon \cdot l(\Gamma(x)) + \int_{\Gamma(x)<0} \left|I(x) - c_1\right|^2 + \int_{\Gamma(x)>0} \left|I(x) - c_2\right|^2 \tag{5}$$

where $l(\Gamma(x))$is the length of the contour $\Gamma(x)$, $\Gamma(x)<0$ represents the region in the image inside the contour which has a mean intensity value c_1, $\Gamma(x)>0$ represents the region in the image outside de contour which has mean intensity value c_2, and υ is a weight to determine the relative influence of the first term. This functional has a minimum when the inside and outside regions in the image are homogeneous and can be represented by their means. Also, the functional penalizes the length of the contour selected, and therefore it is minimal for regions with simpler form.

2.5 Selection of parameters

The main parameter that influences the final outcome of the algorithm is the threshold U in the level set stage. To select this parameter, several segmentations are performed over the image covering a range from 80 to 165. This range was selected evaluating few initial cases and was determined to work for the rest of cases. The final output of the algorithm is selected with the parameter U which minimizes the Mumford Shah functional.

3. MATERIALS AND METHODS

The performance of the algorithm was evaluated with a simulated sonoelastographic image and then applied to *in vivo* thermal lesions produced in a porcine liver.

3.1 Simulations

Two images containing 2 regions each (inclusion and background) were modified to add an arbitrary contrast between the regions. Subsequently, illumination patterns extracted from *in vivo* images were superimposed. A low pass filter was applied to simulate the point spread function expected from sonoelastographic images. Finally, white Gaussian noise is added. The response of the algorithm to different levels of contrast (10, 20, 30 and 40%) was evaluated in terms of the overlap ($A \cap B$ / $A \cup B$) between the segmentation result (A) and the ground truth (B).

3.2 *In vivo* experiments

Eleven RFA lesions and seventeen HIFU lesions were created in eleven porcine livers. In each case, the pig was anesthetized and prepared for surgery. Subsequently, its abdomen was shaved and a laparotomy was performed along the ventral midline and subcostal area to expose the liver. This procedure was performed by the professionals at the Division of Laboratory Animal Medicine (DLAM) following the Animal Use Protocol approved by the University Committee on Animal Resources (UCAR) at the University of Rochester.

For the RFA experiments, an RFA needle (LeVeen needle electrode, Boston Scientific, Natick, MA, USA) was inserted in the liver under US B-mode guidance. The needle was connected to an RF generator (RF 3000 Radiofrequency Ablation System, Boston Scientific, Natick, MA, USA). Following an established treatment algorithm for clinical

practice [20], an RFA lesion was created 1–2 cm beneath the liver surface. In the case of the HIFU experiments, a single-element focused transducer with a focal length of 6 cm and a diameter of 5cm (Model H-101, Sonic Concepts, Inc., Woodinville, WA, USA) was used. The focal intensity of the HIFU transducer is about 1000 W/cm^2. A continuous sinusoidal signal (frequency: 1.1 MHz, voltage: 0.95 V) produced from a function generator (Model 3511A Pragmatic Instruments, San Diego, CA, USA) was fed to a radiofrequency amplifier (Model 2100L, Electronic Navigation Industries, Rochester, NY, USA) which drove the transducer to generate the HIFU beams. The position of the HIFU transducer was adjusted to 4 cm above the liver surface. The water chamber was used as the acoustic coupling between the transducer and the liver surface. The bottom of the water chamber was made of an acoustic transparent film and adjusted to barely touch the liver surface. Within 20 seconds, a single lesion was created. Various-sized lesions were created in the liver by adjusting the duration of HIFU exposure.

Two pistons (Model 2706, Brüel & Kjaer, Naerum, Denmark) were applied directly on the surface of the liver to generate the vibration field needed for sonoelastography. Input signals to the vibration sources were produced by a harmonic waveform generator (Model 3511A Pragmatic Instruments, San Diego, CA, USA) after amplification (Model 2706, Brüel & Kjaer, Naerum, Denmark). The pistons were vibrated at a combination of low frequencies (105, 140, 175 and 210 Hz). Co-registered sonoelastographic and B-mode images were acquired using a linear probe array (M12L) connected to a Logiq 9 US scanner (General Electric Medical Systems, Milwaukee, WI, USA). The position and orientation of the probe over the liver was marked. After imaging, the pig was euthanized and the liver was excised. For each lesion, gross pathology was obtained approximately at the same position and orientation in which it was imaged. Subsequently, gross pathology was photographed and considered to be ground truth.

3.3 Image analysis

Three independent observers measured the area of each of the lesions from the sonoelastographic images using manual segmentation. One observer repeated this procedure three times. The same three observers repeated the process utilizing a semi-automatic segmentation algorithm. Similarly to manual segmentation, one observer measured the lesions three times with the semi-automatic algorithm. From all measurements, interobserver and intraobserver variability was assessed for manual and semi-automatic segmentation. In all cases, the time to perform the segmentation was recorded and the area of the lesions was compared to gross pathology.

4. RESULTS

4.1 Simulations

Figure 2 shows two simulated sonoelastographic images produced with a contrast of 30% before (2a, 2.c) and after (2.b, 2.d) the pre-processing stage of the algorithm. The resulting segmentation from the algorithm for each image is also depicted. In both cases, the selection of the parameter U based on the Mumford Shah functional resulted in the segmentation with higher performance for the tested range. Table 1 presents the performance of the segmentation algorithm for the two simulated images at different contrast levels. As expected, the performance is proportional to the contrast between the inclusion and the background.

4.2 *In vivo* experiments

The diameter of the eleven RFA lesions ranged from 5.8 mm to 20.5 mm, whereas the diameter of the seventeen HIFU lesions ranged from 9.9 mm to 23.3 mm. Table 2 summarizes the results for the RFA and HIFU *in vivo* experiments in terms of accuracy, repeatability and time of segmentation. Results showed that the semi-automatic algorithm outperforms manual segmentation in all aspects evaluated. In particular, the time to measure a lesion reduces significantly from 3.5 minutes to 30 seconds.

The semi-automated algorithm underestimated the diameter of the lesions in 0.4±1.9 mm when compared to manual segmentation. The correlation between both measurements was 80.2%. The error in diameter between the algorithm segmentation and the gross pathology images was 0.95±1.1 mm whereas the manual segmentation error was 1.6±1.3 mm. The correlation between the algorithm and the gross pathology data was 88.7%. The inter- and intra-observer variability for the RFA and HIFU experiments combined was significantly reduced when the algorithm was used. The inter-observer coefficient of variation was decreased from 4.1% to 1.1% and the intra-observer coefficient of variation was lowered from 3.1% to 1.1%. The f-ratios ($\sigma^2_{man} / \sigma^2_{a\lg}$) were 11.3 and 16.6 for the intra-observer and inter-observer cases respectively.

Matched sonoelastographic, B-mode and gross pathology images are presented in Fig. 1. A HIFU lesion is found at the top of the sonoelastographic image. The corresponding B-mode image shows a hyperechoic region due to the gas bubbles formed by the thermal process. The area of the hyperechoic region does not correspond to the area of the actual lesion. The gross pathology image confirms the presence of the lesion.

A comparison between manual and semi-automatic segmentation is illustrated in Fig. 2. Three independent observers manually drew different outlines for the same lesion. The same observers initialized the semi-automatic algorithm by choosing the center of the lesion. Even though they selected different centers, the algorithm produced the same outline.

5. DISCUSSION

Results show that sonoelastography can be used to show and measure thermal ablated lesions. However manual segmentation of the lesions presents challenges in terms of variability and time required. These problems make manual segmentation unfeasible for real-time monitoring of the ablation procedure.

The semi-automatic algorithm presented in this work improves the overall performance of sonoelastography in terms of accuracy and repeatability. In addition, the time to measure the lesion was considerably reduced by a factor of 8 from 3.5 minutes to approximately 25 seconds. Therefore, real-time measurements and monitoring of the lesions are possible. In this context, the algorithm needs to be initialized only at the beginning of the treatment. Subsequently, the resulting outline can be used as the input for the segmentation of the lesion in the following image during the length of the procedure. Template matching has been used previously to automate the initialization step of a segmentation algorithm for compression elastography [14]. In our experiments, this approach fails due to the presence of respiratory and boundary artifacts. Alternatively, in the case of RFA treatment, detection of the RFA needle in B-mode images could be used to initialize the algorithm.

6. CONCLUSION

Our work presents a new approach for semi-automated segmentation of lesions in sonoelastographic images. The algorithm pre-processes the image to compensate for noise and non-uniform vibration fields. The approach is based on fast marching and level set methods. Optimal parameter selection is performed by an adaptive process derived from the Mumford-Shah functional. Resulting segmentations of the algorithm show good agreement with pathology data (r^2=88.7%) and manual segmentation results (r^2=80.2%). More importantly, inter- and intra-observer coefficients of variability are reduced (f-ratios=11.3 and 16.6, respectively) and the time to segment a sonoelastographic image is decreased by a factor of 8 from 3.5 minutes to 25 seconds. Future work will focus on extending the algorithm to three dimensions and on automatic detection of lesions to further minimize human interaction.

ACKNOWLEDGEMENTS

The authors would like to thank Malcolm Bean, Amy Lerner, Art Salo, Peng Wang, Sally Child and Carol Raeman for their suggestions and help. This research was sponsored by the Fischer Fund Grant 4-50275 and by NIH Grant 5 R01 AG016317-07.

REFERENCES

[1] De Sanctis, J.T., Goldberg, S.N., and Mueller P.R., "Percutaneous treatment of hepatic neoplasms: A review of current techniques," Cardiovasc. Intervent. Radiol. 21, 273–296 (1998).

[2] Goldberg, S.N., Gazelle, G.S., and Mueller, P.R., "Thermal ablation therapy for focal malignancy: A unified approach to underlying principles, techniques, and diagnostic imaging guidance," AJR. Am. J. Roentgenol. 174, 323–331 (2000).

[3] Solbiati, L., Ierace, T., Goldberg, S.N., Sironi, S., Livraghi, T., Fiocca R., et al., "Percutaneous US-guided radio-frequency tissue ablation of liver metastases: Treatment and follow-up in 16 patients," Radiol. 202, 195-203 (1997).

[4] Solbiati, L., Goldberg, S.N., Ierace, T., Livraghi, T., Meloni, F., Dellanoce, M., et al., "Hepatic metastases: Percutaneous radio-frequency ablation with cooled-tip electrodes," Radiol. 205, 367-373 (1997).

[5] Zhang, M., "The measurement and imaging of viscoelastic properties of soft tissues and lesions," Ph.D. Dissertation, University of Rochester (2007).
[6] Hindley, J., Gedroyc, W.M., Regan, L., Stewart, E., Tempany, C., Hynyen, K., et al., "MRI guidance of focused ultrasound therapy of uterine fibroids: Early results," AJR. Am. J. Roentgenol., 183, 1713-1719 (2004).
[7] Cha, C.H., Lee, F.T., Gurney, J.M., Markhardt, B.K., Warner, T.F., Kelcz, F., et al., "CT versus sonography for monitoring radiofrequency ablation in a porcine liver," AJR. Am. J. Roentgenol. 175, 705-711 (2000).
[8] Varghese, T., Techavipoo, U., Liu, W., Zagzebski, J.A., Chen, Q., Frank, G., and Lee Jr., F.T., "Elastographic measurement of the area and volume of thermal lesions resulting from radiofrequency ablation: Pathologic correlation," AJR. Am. J. Roentgenol. 181, 701-707 (2003).
[9] Fahey, B.J., Hsu, S.J., Wolf, P.D., Nelson, R.C., and Trahey, G.E., "Liver ablation guidance with acoustic radition force impulse imaging: challenges and opportunities," Physics in Medicine and Biology, 51, 3785-3808 (2006).
[10] Lerner, R.M., Parker, K.J., Holen, J., Gramiak, R., and Waag, R.C., "Sonoelasticity: Medical elasticity images derived from ultrasound signals in mechanically vibrated targets," Acoust. Imaging, 16, 317-327 (1988).
[11] Huang, S.R., Lerner, R.M. and Parker, K.J., "On estimating the amplitude of harmonic vibration from the Doppler spectrum of reflected signals," J. Acoust. Soc. Am., 88, 310-317 (1990).
[12] Fahey, B.J., Dumont, D.M., and Trahey, G.E., "Volume visualization and error analysis using 3D ARFI Imaging Data," Proc. IEEE Ultrasonics symposium (2006).
[13] Techavipoo, U., Varghese, T., Zagzebski, J.A., Chen, Q., and Liu, W., "Semiautomated thermal lesion segmentation for three-dimensional elastographic imaging," Ultrasound in Medicine and Biology, 30, 655-664 (2004).
[14] Liu, W., Zagzebski, J.A., Varghese, T., Dyer, C.R., Techavipoo, U., and Hall, T.J., "Segmentation of elastographic images using a coarse-to-fine active contour model," Ultrasound in Medicine and Biology, 32, 397-408 (2006).
[15] Chan, T.F. and Vese, L.A., "Active contours without edges," IEEE Transactions on Image Processing 10, 266-277 (2001).
[16] Yoo, T., [Insight into images], AK Peters, first edition (2004).
[17] R.F. Gonzalez and R.E. Woods, [Digital Image Processing], Addison-Wesley Pub, third edition (1992).
[18] Sethian, J.A., [Level Set Methods and Fast Marching Methods], Cambridge University Press, second edition (1999).
[19] Ibanez, L., Schroeder, W., Ng, L., and Cates, J., [The ITK software guide], Kitware Inc., first edition (2003).
[20] Curley, S.A., "Radiofrequency ablation of malignant liver tumors," Oncologist. 6, 14-23 (2001).

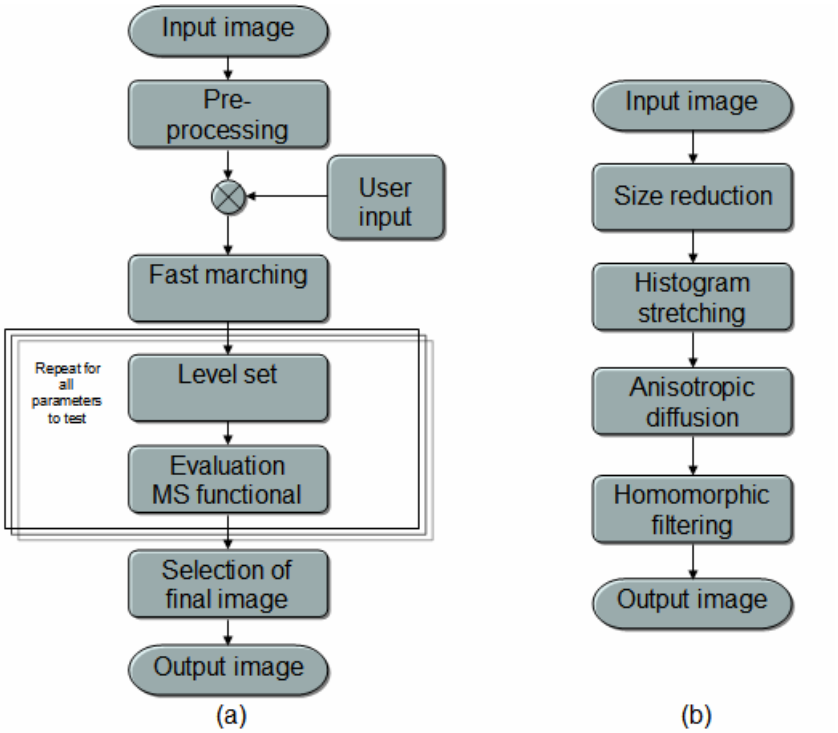

Fig. 1. Flow diagram of the semi-automated algorithm (a) and the pre-processing stage (b).

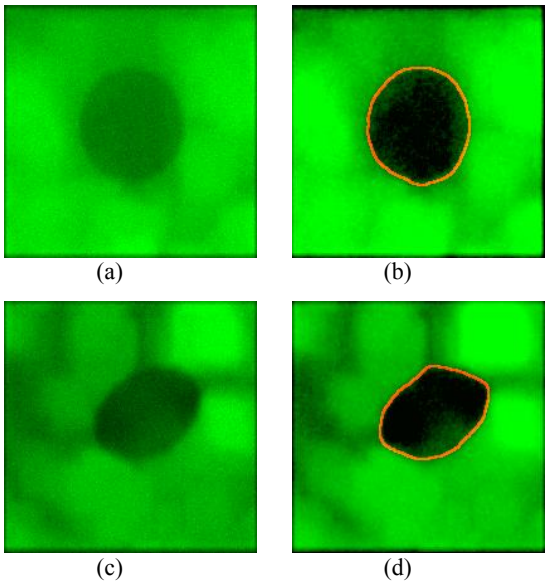

Fig. 2. Simulated sonoelastographic images before (a,c) and after (b,e) pre-processing. The resulting segmentation from the semi-automated algorithm is shown in red.

Table 1. Performance of the algorithm in terms of the percentage of overlap between the resulting segmentation and the ground truth for two simulated lesions.

	10% Contrast	20% Contrast	30% Contrast	40% Contrast
Lesion 1	92.3	94.3	96.4	96.9
Lesion 2	80.3	82.5	87.2	88.7

Table 2. Comparison between manual and semi-automatic segmentations for RFA and HIFU lesions.

	Number of lesions	Correlation coefficient (%)	Average error in equivalent diameter (mm)	Max error in equivalent diameter (mm)	Intra-observer coefficient of variation (%)	Inter-observer coefficient of variation (%)	Average segmentation time per lesion (min)
RFA Lesions							
Manual	11	86.2	1.4	5.9	2.9	5.5	3.9
Algorithm	11	93.1	0.8	2.4	0.4	0.9	0.4
HIFU Lesions							
Manual	14	86.3	2.2	8.2	4.5	5.4	3.2
Algorithm	14	88.7	1.1	5.0	1.0	1.7	0.4

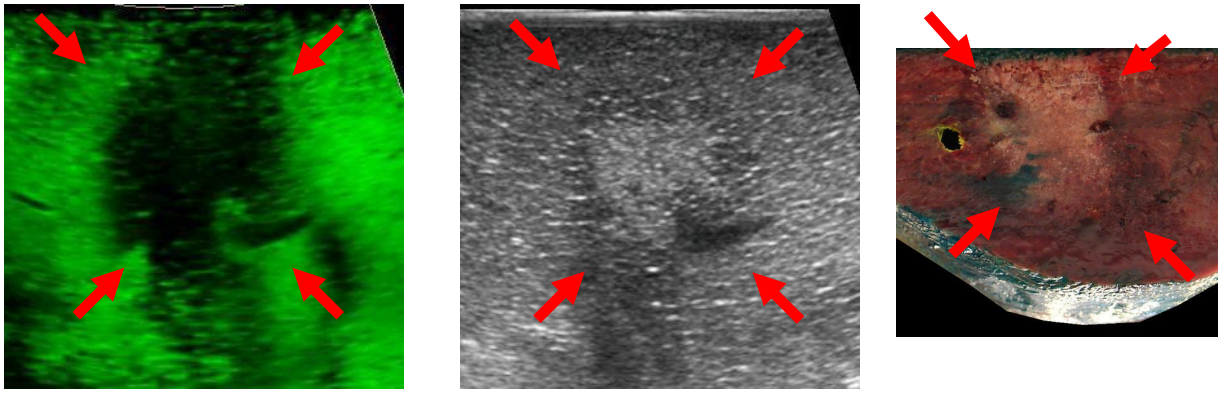

(a) (b) (c)

Fig. 3. Matched (a) sonoelastographic, (b) US B-mode, and (c) Gross pathology images. The red arrows show the HIFU lesion. Note that the hyperechoic region in the B-mode image does not cover the whole area of the lesion

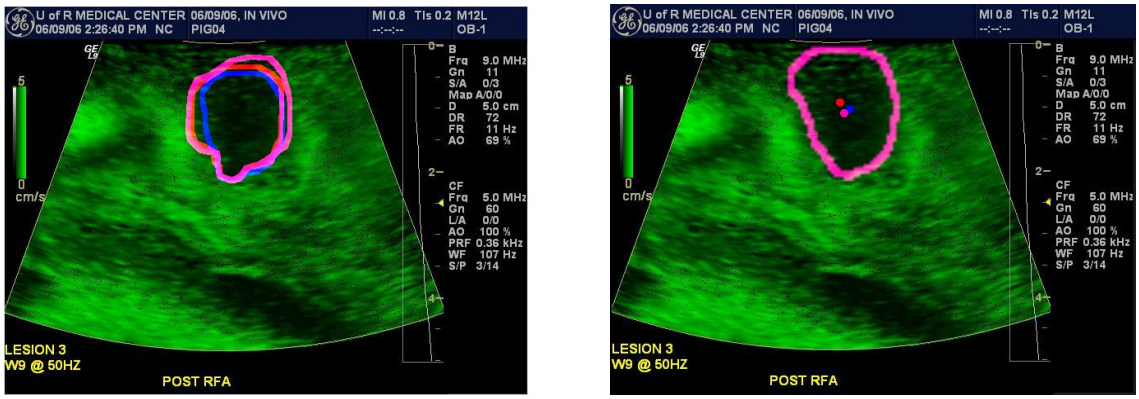

(a) (b)

Fig. 4. Comparison between (a) Manual and (b) Semi-automatic segmentation. Three independent observers (shown in blue, pink and violet) manually outlined the lesion and selected the center of the lesion to initialize the semi-automatic algorithm.